ACS APPLIED ELECTRONIC MATERIALS

pubs.acs.org/acsaelm Article

Electronic Challenges of Retrofitting 2D Electrically Conductive MOFs to Form 3D Conductive Lattices

Khoa N. Le, Jenna L. Mancuso, and Christopher H. Hendon*

Cite This: *ACS Appl. Electron. Mater.* 2021, 3, 2017−2023 Read Online

ACCESS | Metrics & More | Article Recommendations | Supporting Information

ABSTRACT: Porous electrical conductors offer opportunities for next-generation energy storage solutions and electrocatalytic technologies. Metal−organic frameworks are one of the highest porosity scaffolds but typically feature low electrical conductivity due to their highly ionic metal−ligand interface. In this paper, we use computational approaches to study the inclusion of ligating pillars in a known electrically conductive framework, Ni_3(hexaiminobenzene)$_2$. We hypothesize that because Ni_3(hexaiminobenzene)$_2$ is an in-plane conductor, retrofitting this material may yield a 3D-connected network with metallicity in all crystallographic directions. However, we find that while this strategy likely yields unstable connectivity for the Ni^{2+} system, the use of either Cr^{2+} or Fe^{2+} provides a unique avenue to form 3D-connected conductors. The study further highlights the critical role of the metal d_{z^2} orbitals in creating conductive metal−organic frameworks.

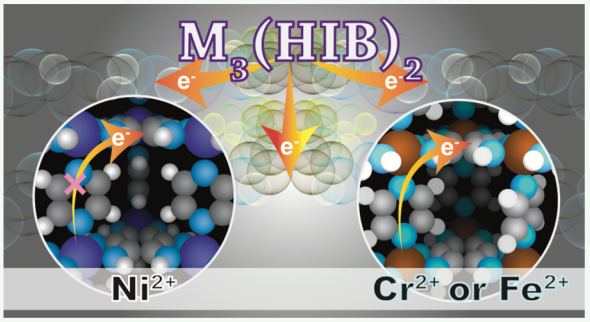

KEYWORDS: *conductivity, metal−organic frameworks, density functional theory, retrofitting*

INTRODUCTION

Metal−organic frameworks (MOFs) are typically celebrated for their ultrahigh surface area[1] and porous geometries,[2] which enable their use as separation[3] and adsorption media[4,5] and site isolated catalysts.[6] Yet, their generally poor electrical conductivity prevents their use in most electronic applications.[7] Efforts to increase the conductivity of MOFs have involved synthesizing novel materials with reduced or zero bandgaps through ligand selection,[8] doping by mixed valency,[9] and defect engineering.[10,11] Although a handful of electrically conductive MOFs have been reported,[12] their conductivities are often below 10^{-2} S/cm, limiting their utility.[13] Increasing MOF conductivity would enable the formation of innovative energy storage and sensing technologies.

In general, electrical conductivity depends on three properties: (i) the number of charge carriers, (ii) their charge, and (iii) their mobility. In insulating, undoped MOFs (i.e., those with discrete bandgaps), the charge carrier mobility is often limited by flat bands arising from the highly ionic metal−ligand interface.[12,14,15] In those cases, the charge of the carriers is ±1 for a hole or electron. Subsequently, several recent studies characterize and quantify the number and identity of the charge carriers, and most examples show increasing conductivity with chemical oxidation, that is, the formation of holes.[16,17] Yet, the mobility and directionality of conduction are still limited by the scaffold geometry.[18]

The highest performing MOF conductors do not feature an explicit bandgap: in other words, the MOFs are metallic. These scaffolds (e.g., Ni_3(HITP)$_2$,[19] Ni_3(HIB)$_2$,[20] etc.[21]) feature more covalent metal−ligand bonds. Similar to graphitic materials,[22] the π-orbitals from the linkers create delocalized bands that exhibit dispersion both in and out of the covalently connected plane.

Yet, the electronic structure of 2D metal−organic graphene analogues is nuanced. There is increasing evidence to suggest that the linkers are oxidized during the formation of these MOFs, rendering them no longer aromatic.[23−28] Considering the most well-studied 2D conductive MOF, Ni_3(HITP)$_2$ (HITP ≡ 2,3,6,7,10,11-hexaiminotriphenylene),[29−35] each HITP linker must be assigned a formal oxidation state of 3− to satisfy the charge neutrality condition. Therefore, each linker would host an odd number of electrons (assuming a single deprotonation has occurred for each amine). However, previous work has elucidated that a monolayer of this material features a discrete bandgap and no unpaired electrons.[36] Each pair of linkers can therefore be thought of as a closed-shell −4/−2 pair (a resonance structure of −3/−3): a Robin−Day Class III system.[37]

While the monolayer features a narrow but discrete bandgap, metallicity is observed in the bulk vdW form (where weak dispersion interactions between stacked linkers arise from π-

Received: December 28, 2020
Accepted: April 19, 2021
Published: April 29, 2021

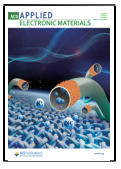

https://doi.org/10.1021/acsaelm.0c01135
ACS Appl. Electron. Mater. 2021, 3, 2017−2023

orbital overlap).[38] This manifests as the emergence of metallic bands in the bulk electronic band structure along the out-of-plane (π-stacked) $\Gamma-Z$ vector (Figure S1). Broadly, linker-based radicals are thought to be stabilized by two mechanisms: (i) formation of a curved (disperse) band in-plane, delocalizing the electrons within the covalent sheet, and (ii) formation of a curved band out-of-plane, delocalizing the electrons in the vdW direction.

Another consideration for these 2D analogues is the range of accessible sheet stacking arrangements. The potential energy surface of sheet slipping in $Ni_3(HITP)_2$ is shallow; with a penalty of <0.7 eV for all parallel-displaced configurations[29] the pores could be thermally distorted by sheets slipping up to ~0.1 nm in the a/b plane under ambient conditions. The pores could be further occluded by sheets slipping past one another, perhaps under extreme conditions (e.g., high heat and pressure). While the implications for electrical conductivity appear to be minimal based on these partially sheet-slipped band structures,[38] diminished porosity undermines MOF utility for energy storage applications.

One emergent strategy to maintain the porosity of conductive 2D MOFs is to strengthen the intersheet interactions via retrofitting (a form of postsynthetic ligand modification[39,40] known to affect both the electronic and structural properties of materials[41−43]). The general concept is that the sheets can be held in place by installing a linker to connect the formally square planar Ni^{2+}, yielding octahedral Ni^{2+} and a 3D-connected scaffold. In a recent study, Foster and colleagues demonstrated that the installation of such pillars in $Ni_3(HITP)_2$ created a wide bandgap material,[38] highlighting the importance of d_{z^2} orbitals on the metals in facilitating Class III delocalization of the ligand. In other words, the pillars destroyed the out-of-plane covalency and resulted in a semiconductor. Thus, the results showed that retrofitting a MOF whose monolayer features a bandgap seems to yield a 3D-connected insulator.

Here, we examine a different family of 2D MOF conductors based on a recently reported structure, $Ni_3(HIB)_2$ (HIB ≡ hexaiminobenzene).[20] Unlike the triphenylene-based materials, the monolayer is metallic.[36] The three-electron oxidation of triphenylene can be thought of as yielding a relatively stable quinone monoradical.[29] We believe metallicity emerges in $Ni_3(HIB)_2$ because the same three electron oxidation of a single benzene ring results in a half-populated HIB band, which by definition is metallic. The bulk material is also metallic with metallically dispersed bands in the a/b plane, independent of sheet stacking configuration (see the M−Γ−K vectors in Figure 1). We have previously studied and contrasted $Ni_3(HITP)_2$ and $Ni_3(HIB)_2$,[36] revealing dissimilarities in their electronic structure motivated by the in-plane metallicity of the latter.

Metallicity in $Ni_3(HIB)_2$ monolayer makes bulk metallicity independent of the stacking orientation and intersheet spacing. In contrast, $Ni_3(HITP)_2$ conducts primarily out-of-plane, and increasing intersheet spacing hinders charge transport throughout the material. Resultantly, the previous 2D to 3D retrofitting study turns a 2D conductive MOF into a 3D semiconductor by reducing band dispersion and introducing a bandgap. Instead, we propose modifying $Ni_3(HIB)_2$, allowing the formation of 3D MOFs that retain the metallic character of the 2D MOF.

This paper introduces intersheet bridging linkers into $Ni_3(HIB)_2$ that induce a change in metallicity and band dispersion of the newly formed 3D-connected material. We show that while this procedure does yield a metal, it is likely due to material instability rather than the desired retrofitted 3D conductor. To overcome this challenge, we propose alternative compositions that may be more thermodynamically accessible. This study further emphasizes the importance of the d_{z^2} orbital occupancy in forming disperse bands and stable MOF conductors.

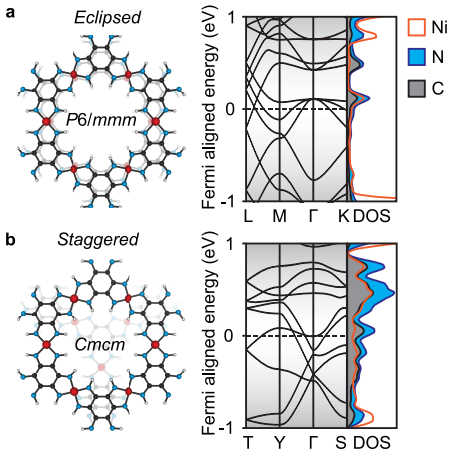

Figure 1. $Ni_3(HIB)_2$ is a bulk metal, independent of sheet slipping. Yet, greater band dispersion for eclipsed stacking structure (a) in the out-of-plane direction (L−M) compared to that of the staggered counterpart (b) for $Ni_3(HIB)_2$.

RESULTS AND DISCUSSION

Eclipsed versus Staggered $Ni_3(HIB)_2$ Models. While the absolute electronic structure of individual HIB linkers depends on the extent of oxidation, the σ-bonding network within each ligand remains intact. Thus, we term this direction the "covalent plane". These sheets are held together by much weaker electrostatic interactions between the layers—we term this direction "out-of-plane". Bulk electronic properties depend on the sheet stacking orientations (Figure 1). When these 2D sheets are in their eclipsed stacking conformation, one would expect the overlap between organic π-orbitals of adjacent layers to be maximized, along with the repulsion of Ni d_{z^2} orbitals. Deviation from the eclipsed stacking structure reduces the orbital overlap and therefore band dispersion in this direction. This effect is reflected in the k-path from L-to-M and T-to-Y (out-of-plane). However, the impact of stacking conformations on the band dispersion in the covalent plane is not as clear (see the k-path M−Γ−K and Y−Γ−S). Regardless, both staggered and eclipsed conformations are persistently metallic, as evidenced by the band crossing the computed Fermi level and the nonzero density of states (DOS).

The eclipsed structure is, however, energetically disfavored by ~6 kcal/mol (Figure 2a). At the interlayer distance of ~3.36 Å—the experimentally reported interlayer distance for this framework[20]—it is unlikely for $Ni_3(HIB)_2$ to obtain the eclipsed structure. As we artificially exfoliate the layers by progressively stepping them apart, both forms converge to the energy of a free monolayer. Interestingly, however, the eclipsed structure exhibits the most disfavored orientation at an interlayer distance of ~5 Å, suggesting that eclipsed layers may be metastable (see also the absence of imaginary frequency in Table S1).

Increasing interlayer spacing reduces the electrostatic interaction between the sheets. Therefore, the metallicity is

https://doi.org/10.1021/acsaelm.0c01135
ACS Appl. Electron. Mater. 2021, 3, 2017−2023

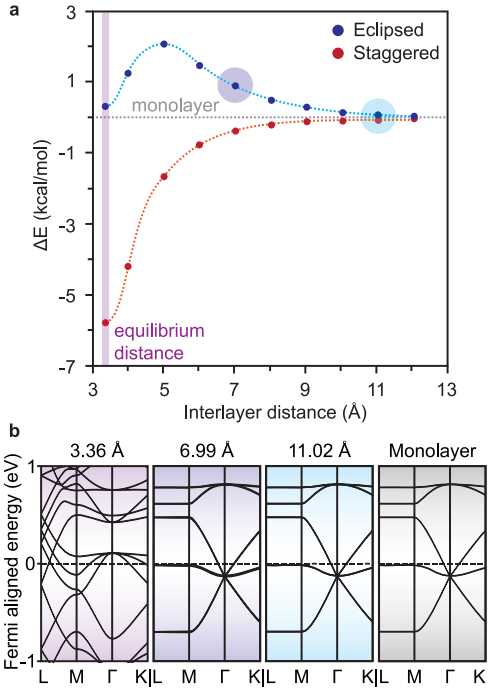

Figure 2. (a) Relative energy of bulk structure of $Ni_3(HIB)_2$ in staggered (red) and eclipsed (blue) conformation compare to that of monolayer (gray). (b) Band structures of $Ni_3(HIB)_2$ in eclipsed conformation (first three panels) and $Ni_3(HIB)_2$ monolayer (gray). The interlayer spacings are show above the corresponding panels.

diminished in the out-of-plane direction, as shown in Figure 2b (see the flattening of the bands from L-to-M at the interlayer distance of 6.99 and 11.02 Å). The *k*-path M−Γ−K reveals the impact on the electronic properties of the material in the covalent plane. Although the increase in interlayer distance reduces the number of bands crossing the Fermi level, the metallicity of the material remains unchanged (shown in Figure 2b). Still, we do not know whether the addition of an axial ligand to the Ni^{2+} atoms will be energetically preferable to forming the bulk 2D material.

Retrofitting Square-Planar Ni^{2+}. We seek to link the coordinatively unsaturated nodes of metallic $Ni_3(HIB)_2$ monolayers by using extrinsic ligands. Three potential bridging organic linker candidates are explored: 1,4-pyrazine, DABCO (1,4-diazabicyclo[2.2.2]octane), and 4,4′-bipyridine, all of which are commonly used linkers in the MOF field.[44−46] Retrofitting these linkers results in interlayer spacing of 7 Å (pyrazine), ∼9 Å (DABCO), and ∼11 Å (bipyridine). In each case, the sheets are sufficiently far apart (per Figure 2b) to minimize π-stacking interactions between the covalent sheets.

The 3D-connected retrofitted structures of $Ni_3(HIB)_2$ are shown in Figure 3. First, we consider the effect of a pure σ-donor linkage through the inclusion of DABCO (Figure 3a). From an energetic perspective, the DABCO linkers insertion was thermodynamically disfavored by 2.30 kcal/mol (Table 1). Our phonon calculations revealed imaginary frequencies in the geometrically equilibrated structures, suggesting the material is not dynamically stable. We also noted that the DABCO−Ni bond length converged to 3.06 Å (beyond what any reasonable metal−ligand bond might be), so we employed the density-derived electrostatic and chemical approach (DDEC)[47] to evaluate the bond orders for these bonds. The metal−ligand bond order in the out-of-plane direction is 0.07, which is very

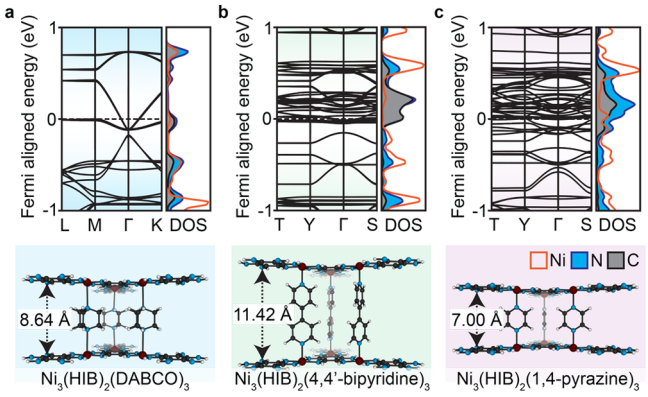

Figure 3. Effect of bridging linkers insertion on band structures of $Ni_3(HIB)_2$ frameworks: (a) pyrazine (purple), (b) DABCO (blue), and (c) bipyridine (green). The corresponding 3D structure is shown below each of the band structures and DOS.

Table 1. Relative Energy of Formation for Bipyridine, Pyrazine, and DABCO Retrofitted into $M_3(HIB)_2$ Frameworks (Energies Are Presented in kcal/mol)

	Ni	Cr	Fe
4,4′-bipyridine	61.85	−110.42	−81.23
1,4-pyrazine	68.61	−115.64	−74.20
DABCO	2.30	−64.49	−23.99

weak compared to the in-plane metal−NH bond (bond order of 0.78, bond length of 1.82 Å). For comparison, the bond orders in nonretrofitted $Ni_3(HIB)_2$ bulk and monolayer Ni−NH bonds are 0.78 and 0.84, respectively. The decreasing bond order in bulk $Ni_3(HIB)_2$ compared to that of the monolayer is one avenue to assess the importance of the vdW stacking. Considering the long DABCO−Ni bond, the band structure remains very similar to that of the monolayer (Figure 3a), which further indicates that the DABCO linkers are likely not interacting with the $Ni_3(HIB)_2$ layers. We attribute this to square-planar Ni^{2+} being a weak Lewis acid and axial ligation forming high-spin octahedral Ni^{2+}. Because the d_{z^2} orbital is formally occupied in the square-planar complex, σ-donor ligands form a nonbonding interaction.

Both pyrazine and 4,4′-bipyridine are σ-donors but better π-acceptors than DABCO. Retrofitted $Ni_3(HIB)_2(1,4\text{-pyrazine})_3$ and $Ni_3(HIB)_2(4,4'\text{-bipyridine})_3$ result in metal−ligand bond lengths of 2.11 and 2.15 Å for the pyrazine and bipyridine analogues, respectively (Figure 3b,c). In the former, a bond order of 0.38 was found for the metal−ligand bond in the out-of-plane direction, which is relatively low compared to the in-plane metal ligation (bond order 0.53). Similarly, for $Ni_3(HIB)_2(4,4'\text{-bipyridine})_3$, a bond order of 0.36 was found for the metal−ligand bond in the out-of-plane direction (compared to a bond order of 0.52 for the metal−ligand bond in the covalent plane). The inclusion of a π-acceptor dramatically reduces the in-plane bonding interactions. As a result, these inclusions are highly energetically unfavorable: the insertion of bipyridine and pyrazine linkers into the framework increases the Gibbs free energy by 61.85 and 68.61 kcal/mol, respectively (Table 1). Again, the presence of imaginary frequencies revealed that these structures are not dynamically stable (Table S1).

In sum, a retrofitting approach using only σ-donors results in the Ni-MOF preferring nonbonded (or simply intercalated)

https://doi.org/10.1021/acsaelm.0c01135
ACS Appl. Electron. Mater. 2021, 3, 2017−2023

pillars. The π-accepting ligands result in a bond, but at extreme energetic penalty due to reorganization of the Ni^{2+} d orbitals, inhibiting the binding of fifth and sixth axial ligands. Hence, retrofitting $Ni_3(HIB)_2$ with the pillars creates unstable materials, independent of their properties.

Transmetalation. Given the energetic penalty of creating octahedral Ni^{2+}, we now examine the possibility of altering metal composition to minimize the d_{z^2} repulsive interaction. To do so, we expand our study to include other divalent transition metals in the form of $Cu_3(HIB)_2$, $Fe_3(HIB)_2$, and $Cr_3(HIB)_2$. The Cu^{2+} material has been previously synthesized,[20] but it is also a late transition metal with filled d_{z^2} orbitals. We hypothesized that retrofitted $Cu_3(HIB)_2$ would exhibit similar properties to $Ni_3(HIB)_2$ since they have filled d_{z^2} orbitals. Indeed, our attempt to obtain a model for $Cu_3(HIB)_2(DABCO)_3$ resulted in much the same as we observed for the Ni^{2+} system—intercalated and nonbonding. As a result, we turned our interest to the Cr^{2+} and Fe^{2+} systems.

We selected Fe^{2+} and Cr^{2+} because it allows us to depopulate the valence orbitals in steps while minimizing the computational difficulties of computing magnetic ordering of other first-row transition metals (e.g., Mn^{2+} and Co^{2+}). In addition, both Cr^{2+} and Fe^{2+} form high-spin complexes in square-planar coordination spheres, leaving the d_{z^2} orbitals partially filled. The partially filled d_{z^2} orbitals can readily accept extra electrons from the bridging linkers to form octahedral coordination spheres. Additionally, both Fe and Cr have been used in the formation of MOFs.[48,49]

The electronic band structures of eclipsed $Fe_3(HIB)_2$ and $Cr_3(HIB)_2$ are presented in Figure 4. These 2D-connected

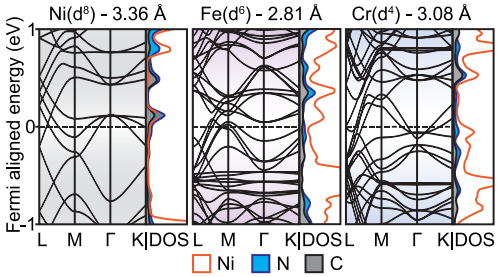

Figure 4. Band structures of eclipsed $M_3(HIB)_2$ showing all materials are metallic and the band remain dispersive near the Fermi level for all metal identity.

materials show similar band dispersion behavior to that of the nickel analogue; bands cross the computed Fermi level in both the out-of-plane and the covalent plane directions. As expected, the increased interlayer distance also flattened the band dispersion in the out-of-plane direction (see Figure 5).

Retrofitting Cr- and Fe-HIB Derivatives. The retrofitted MOFs yield metal−axial ligand bond lengths of 1.95 Å (pyrazine), 1.98 Å (bipyridine), 2.16 Å (DABCO) for Fe^{2+} analogues, and 2.04 Å (pyrazine), 2.06 Å (bipyridine), and 2.24 Å (DABCO) for the Cr^{2+} analogues. The formation of a bonding interaction between DABCO with Cr^{2+} and Fe^{2+} metal centers clearly shows that earlier transition metals can form pure σ-bonding interaction with axial linkers. Furthermore, there is a slight elongation of the in-plane Fe^{2+} bonds after retrofitting (compared to the nonretrofitted structure, see Table S2) which can be rationalized by increased e^- density associated with the metal repulsing the M−pillar bond.

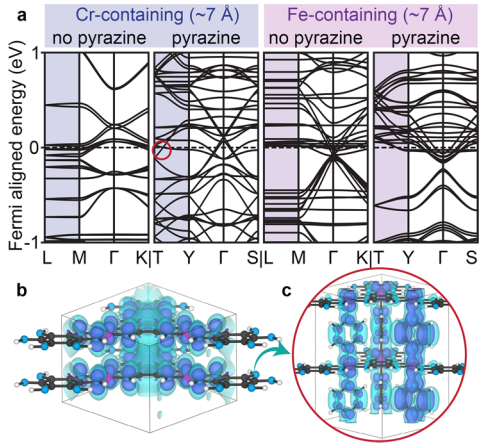

Figure 5. (a) Effect of pyrazine insertion on the band structure of $Cr_3(HIB)_2$ and $Fe_3(HIB)_2$. (b) Charge density of a dispersive band that gave rise to out-of-plane metallicity in 2D eclipsed bulk $Cr_3(HIB)_2$ due to orbital overlap. (c) Charge density of dispersive band that gave rise to out-of-plane metallicity in $Cr_3(HIB)_2(1,4\text{-pyrazine})_3$ due to covalent interaction in the axial direction.

The bond orders for the metal−axial ligands were computed to be 0.32 (DABCO), 0.53 (pyrazine), and 0.51 (bipyridine) for the Fe^{2+} analogues and 0.27 (DABCO), 0.45 (pyrazine), and 0.42 (bipyridine) for the Cr^{2+} analogues. These bond orders are somewhat smaller than those computed for the metal−ligand bonds in the covalent direction (approximately 0.1−0.2 lower for pyrazine and bipyridine linkers and 0.3−0.4 lower for DABCO linker, Table S2). These weaker (longer) bonds result from the nonuniform distribution of electron density between metal orbitals and the in-plane and out-of-plane ligands due to their different shape and orientation.[50] These factors contribute to the Jahn−Teller distortion observed in the coordination sphere of our retrofitted structures, which commonly occurs for octahedral complexes.[51,52] The metal−axial ligand bond orders for $Fe_3(HIB)_2(DABCO)_3$ and $Cr_3(HIB)_2(DABCO)_3$ are small but still support the existence of a σ-bond interaction between the DABCO linker and the Fe^{2+} and Cr^{2+} metal centers. The formation of these axial metal−ligand bonds is supported by the observed Jahn−Teller distortions and the decrease in bond order of the metal−ligand bonds in the covalent direction. This decrease in bond order is not observed for the $Ni_3(HIB)_2(DABCO)_3$ structure, where the metal−axial ligand bond order is significantly smaller (0.07).

The electronic band structures of the 3D retrofitted MOFs (for Cr and Fe) show the retainment of band dispersion in the covalent direction after bridging linker insertion (M−Γ−K, Figure 5). Interestingly, for these earlier transition metals, retrofitting also allows the materials to regain dispersion in the out-of-plane direction without the $\pi-\pi$ orbital interactions that exist between the layers when they were closer to each other: an example is shown in Figure 5a, T−Y, along with the charge density comparison before and after retrofitting in Figure 5b,c. Electronic band structures for other retrofitted MOFs depicting similar results can be found in Figure S2. This out-of-plane covalency is due to the metal−axial ligand bonding interaction (formed from σ-type interactions hindered by d_{z^2} occupancy in Ni^{2+} analogues). Our calculations suggest that the σ-bond interaction allows delocalization of charge in the out-of-plane direction via the through-bond charge transport

https://doi.org/10.1021/acsaelm.0c01135
ACS Appl. Electron. Mater. 2021, 3, 2017−2023

pathway. In $Cr_3(HIB)_2$(1,4-pyrazine)$_3$, the partial charge density from the dispersive, metallic band in the out-of-plane direction (shown in Figure 5c) reveals the Cr−pyrazine bonding interaction. A similar interaction was present in the Fe^{2+} analogue but was not observed in the Ni^{2+} analogue, which possesses flatter bands in the out-of-plane direction (see Figure 3c).

In sum, all metal−axial ligand bond orders for the Fe- and Cr-based retrofitted MOFs are large compared to the Ni-based retrofitted MOFs. Early transition metals are better retrofitting candidates because they allow both σ-donation and π-backbonding interactions from the axial linkers. Furthermore, the formation energies of these 3D retrofitted MOFs from their 2D parent frameworks are largely negative (Table 1), indicating that for Cr^{2+} and Fe^{2+} forming octahedral coordination spheres from their initial square-planar coordination spheres is energetically favorable. Unfortunately, phonon calculations for some of the retrofitted 3D MOFs reveal imaginary frequencies (see Table S1). These negative modes would suggest that corresponding structures may not be thermodynamically metastable. However, these frequencies may instead correspond to artificial ring rotations between the retrofitted linkages, particularly given the formation energies are so favorable.

CONCLUSIONS

Together, our study demonstrates that 3D conductive MOFs can be generated by retrofitting covalent 2D sheets that house square planar metals with partially, or unoccupied, d_{z^2} orbitals using neutral N-donor pillar ligands. The $Ni_3(HIB)_2$ framework exhibits more dispersive bands, especially in the out-of-plane direction, when adopting the eclipsed stacking conformation. However, the eclipsed structure is energetically unfavorable compared to the staggered configuration. Because of d_{z^2} orbital occupancy, retrofitting the $Ni_3(HIB)_2$ scaffold with bipyridine, pyrazine, and DABCO generates thermodynamically destabilized structures. However, incorporating transition metals with reduced d_{z^2} density form bonding interactions with both DABCO and the aromatic linkages. The resulting materials are thermodynamically stable and potentially dynamically metastable. Although direct synthesis of the Cr and Fe analogues ($Fe_3(HIB)_2$ and $Cr_3(HIB)_2$) may not be tractable, ligand pillaring approaches and metal exchange may afford synthetic access to these structures and the emergence of a novel class of 3D-connected electrical conductors.

COMPUTATIONAL METHODS

Structural equilibration of both the eclipsed and staggered $Ni_3(HIB)$ was performed with DFT as implemented in the Vienna *ab initio* Simulation Package (VASP, ver. 5.4.4).[53] The structures were relaxed by using the unrestricted GGA-PBEsol exchange−correlation functional.[54] Ionic relaxation was achieved when all forces were smaller than 0.005 eV Å^{-1}. The plane-wave cutoff was set at 500 eV, and the SCF convergence criterion was 10^{-6} eV. An automatically generate k-grid was used during the optimization with 2 × 2 × 4 sampling meshes. Symmetry was not enforced in the case of Jahn−Teller or other distortions. The interlayer distances were then increased from 3.3 to 12 Å at 1 Å increments. Each structure was then fully equilibrated with a constant volume but variable ionic positions and lattice parameters to create the potential energy surfaces in the noncovalent direction. Retrofitting was then performed by adding pyrazines, DABCO, and bipyridine linkers in the eclipsed structure. These structures were then equilibrated by using the same criteria. Other metal derivatives were created by substituting Ni and converged by using the same parameters.

All optimized structures were used for electronic band structures and corresponding density-of-states calculations at the GGA-PBEsol level of theory since all materials are metallic, and qualitative analysis of band curvature is not thought to change dramatically by using a hybrid functional in this case.[18] Additionally, PBEsol significantly reduced the computational expense. GGA+*U* calculations and HSE06 functionals were also explored on the bulk staggered structure of $Ni_3(HIB)_2$ to clarify that GGA-PBEsol functional is sufficient for this study. Two *U* parameters were selected (3 and 6.2 eV) as recommended by the literature on related materials.[34,55,56]

Phonon modes and frequencies were obtained via the finite differences method as implemented in VASP at the zone-center (Γ-point). Central difference was enforced, and the step size was set to be 0.015 Å as default. The unrestricted GGA-PBEsol exchange-correlation functional was used with the same convergence criteria as above.

ASSOCIATED CONTENT

Supporting Information

The Supporting Information is available free of charge at https://pubs.acs.org/doi/10.1021/acsaelm.0c01135.

Extended computational details (PDF)
Equilibrium geometry files for all models (ZIP)

AUTHOR INFORMATION

Corresponding Author

Christopher H. Hendon − *Department of Chemistry and Biochemistry, University of Oregon, Eugene, Oregon 97403, United States;* orcid.org/0000-0002-7132-768X; Email: chendon@uoregon.edu

Authors

Khoa N. Le − *Department of Chemistry and Biochemistry, University of Oregon, Eugene, Oregon 97403, United States*

Jenna L. Mancuso − *Department of Chemistry and Biochemistry, University of Oregon, Eugene, Oregon 97403, United States*

Complete contact information is available at: https://pubs.acs.org/10.1021/acsaelm.0c01135

Author Contributions

K.N.L. and C.H.H. performed the experiments. All authors contributed to writing the manuscript.

Notes

The authors declare no competing financial interest.

ACKNOWLEDGMENTS

Computational studies were performed by using the High-Performance Computing cluster at the University of Oregon (Talapas), the Extreme Science and Engineering Discovery Environment (XSEDE), which is supported by National Science Foundation Grant ACI-1548562, and the Portland State University machine, Coeus, which is supported by the NSF (DMS1624776). C.H.H. is supported in part by the National Science Foundation under Grant DMR-1956403. K.N.L. is supported by the National Science Foundation Graduate Research Fellowship under Grant 1650114.

REFERENCES

(1) Farha, O. K.; Eryazici, I.; Jeong, N. C.; Hauser, B. G.; Wilmer, C. E.; Sarjeant, A. A.; Snurr, R. Q.; Nguyen, S. T.; Yazaydın, A. Ö.; Hupp, J. T. Metal-Organic Framework Materials with Ultrahigh

Surface Areas: Is the Sky the Limit? *J. Am. Chem. Soc.* **2012**, *134*, 15016−15021.
(2) Schoedel, A.; Yaghi, O. M. Porosity in Metal-Organic Compounds. In *Macrocyclic and Supramolecular Chemistry*; Izatt, R. M., Ed.; John Wiley & Sons, Ltd.: Chichester, UK, 2016; pp 200−219.
(3) Li, J.-R.; Sculley, J.; Zhou, H.-C. Metal-Organic Frameworks for Separations. *Chem. Rev.* **2012**, *112*, 869−932.
(4) Ghanbari, T.; Abnisa, F.; Wan Daud, W. M. A. A Review on Production of Metal Organic Frameworks (MOF) for CO_2 Adsorption. *Sci. Total Environ.* **2020**, *707*, 135090.
(5) Petit, C. Present and Future of MOF Research in the Field of Adsorption and Molecular Separation. *Curr. Opin. Chem. Eng.* **2018**, *20*, 132−142.
(6) Corma, A.; García, H.; Llabrés i Xamena, F. X. Engineering Metal Organic Frameworks for Heterogeneous Catalysis. *Chem. Rev.* **2010**, *110*, 4606−4655.
(7) Kung, C.-W.; Han, P.-C.; Chuang, C.-H.; Wu, K. C.-W. Electronically Conductive Metal-Organic Framework-Based Materials. *APL Mater.* **2019**, *7*, 110902.
(8) Degaga, G. D.; Pandey, R.; Gupta, C.; Bharadwaj, L. Tailoring of the Electronic Property of Zn-BTC Metal-Organic Framework via Ligand Functionalization: An Ab Initio Investigation. *RSC Adv.* **2019**, *9*, 14260−14267.
(9) Park, J. G.; Aubrey, M. L.; Oktawiec, J.; Chakarawet, K.; Darago, L. E.; Grandjean, F.; Long, G. J.; Long, J. R. Charge Delocalization and Bulk Electronic Conductivity in the Mixed-Valence Metal-Organic Framework $Fe(1,2,3\text{-Triazolate})_2(BF_4)_x$. *J. Am. Chem. Soc.* **2018**, *140*, 8526−8534.
(10) Bueken, B.; Van Velthoven, N.; Krajnc, A.; Smolders, S.; Taulelle, F.; Mellot-Draznieks, C.; Mali, G.; Bennett, T. D.; De Vos, D. Tackling the Defect Conundrum in UiO-66: A Mixed-Linker Approach to Engineering Missing Linker Defects. *Chem. Mater.* **2017**, *29*, 10478−10486.
(11) Dissegna, S.; Epp, K.; Heinz, W. R.; Kieslich, G.; Fischer, R. A. Defective Metal-Organic Frameworks. *Adv. Mater.* **2018**, *30*, 1704501.
(12) Xie, L. S.; Skorupskii, G.; Dincă, M. Electrically Conductive Metal-Organic Frameworks. *Chem. Rev.* **2020**, *120*, 8536−8580.
(13) N, N.; Maity, K.; Saha, S. Electrically Conductive Metal-Organic Frameworks. *In Elaboration and Applications of Metal-organic Frameworks* **2018**, 655−686.
(14) Hendon, C. H.; Rieth, A. J.; Korzyński, M. D.; Dincă, M. Grand Challenges and Future Opportunities for Metal-Organic Frameworks. *ACS Cent. Sci.* **2017**, *3*, 554−563.
(15) Walsh, A.; Butler, K. T.; Hendon, C. H. Chemical Principles for Electroactive Metal-Organic Frameworks. *MRS Bull.* **2016**, *41*, 870−876.
(16) Clough, A. J.; Orchanian, N. M.; Skelton, J. M.; Neer, A. J.; Howard, S. A.; Downes, C. A.; Piper, L. F. J.; Walsh, A.; Melot, B. C.; Marinescu, S. C. Room Temperature Metallic Conductivity in a Metal-Organic Framework Induced by Oxidation. *J. Am. Chem. Soc.* **2019**, *141*, 16323−16330.
(17) Bhardwaj, S. K.; Bhardwaj, N.; Kaur, R.; Mehta, J.; Sharma, A. L.; Kim, K.-H.; Deep, A. An Overview of Different Strategies to Introduce Conductivity in Metal-Organic Frameworks and Miscellaneous Applications Thereof. *J. Mater. Chem. A* **2018**, *6*, 14992−15009.
(18) Mancuso, J. L.; Mroz, A. M.; Le, K. N.; Hendon, C. H. Electronic Structure Modeling of Metal-Organic Frameworks. *Chem. Rev.* **2020**, *120*, 8641−8715.
(19) Nguyen, D. K.; Schepisi, I. M.; Amir, F. Z. Extraordinary Cycling Stability of $Ni_3(HITP)_2$ Supercapacitors Fabricated by Electrophoretic Deposition: Cycling at 100,000 Cycles. *Chem. Eng. J.* **2019**, *378*, 122150.
(20) Dou, J.-H.; Sun, L.; Ge, Y.; Li, W.; Hendon, C. H.; Li, J.; Gul, S.; Yano, J.; Stach, E. A.; Dincă, M. Signature of Metallic Behavior in the Metal-Organic Frameworks $M_3(Hexaiminobenzene)_2$ (M = Ni, Cu). *J. Am. Chem. Soc.* **2017**, *139*, 13608−13611.
(21) Dong, R.; Zhang, Z.; Tranca, D. C.; Zhou, S.; Wang, M.; Adler, P.; Liao, Z.; Liu, F.; Sun, Y.; Shi, W.; Zhang, Z.; Zschech, E.; Mannsfeld, S. C. B.; Felser, C.; Feng, X. A Coronene-Based Semiconducting Two-Dimensional Metal-Organic Framework with Ferromagnetic Behavior. *Nat. Commun.* **2018**, *9*, 2637.
(22) Kim, K. K.; Kim, S. M.; Lee, Y. H. Chemically Conjugated Carbon Nanotubes and Graphene for Carrier Modulation. *Acc. Chem. Res.* **2016**, *49*, 390−399.
(23) Stiefel, E. I.; Waters, J. H.; Billig, E.; Gray, H. B. The Myth of Nickel(III) and Nickel(IV) in Planar Complexes [1]. *J. Am. Chem. Soc.* **1965**, *87*, 3016−3017.
(24) Herebian, D.; Bothe, E.; Neese, F.; Weyhermüller, T.; Wieghardt, K. Molecular and Electronic Structures of Bis-(o-Diiminobenzosemiquinonato)Metal(II) Complexes (Ni, Pd, Pt), Their Monocations and -Anions, and of Dimeric Dications Containing Weak Metal-Metal Bonds. *J. Am. Chem. Soc.* **2003**, *125*, 9116−9128.
(25) Dou, J.-H.; Arguilla, M. Q.; Luo, Y.; Li, J.; Zhang, W.; Sun, L.; Mancuso, J. L.; Yang, L.; Chen, T.; Parent, L. R.; Skorupskii, G.; Libretto, N. J.; Sun, C.; Yang, M. C.; Dip, P. V.; Brignole, E. J.; Miller, J. T.; Kong, J.; Hendon, C. H.; Sun, J.; Dincă, M. Atomically Precise Single-Crystal Structures of Electrically Conducting 2D Metal-Organic Frameworks. *Nat. Mater.* **2021**, *20*, 222−228.
(26) Day, R. W.; Bediako, D. K.; Rezaee, M.; Parent, L. R.; Skorupskii, G.; Arguilla, M. Q.; Hendon, C. H.; Stassen, I.; Gianneschi, N. C.; Kim, P.; Dincă, M. Single Crystals of Electrically Conductive Two-Dimensional Metal-Organic Frameworks: Structural and Electrical Transport Properties. *ACS Cent. Sci.* **2019**, *5*, 1959−1964.
(27) Stassen, I.; Dou, J.-H.; Hendon, C.; Dincă, M. Chemiresistive Sensing of Ambient CO_2 by an Autogenously Hydrated Cu3-(Hexaiminobenzene)2 Framework. *ACS Cent. Sci.* **2019**, *5*, 1425−1431.
(28) Yang, L.; He, X.; Dincă, M. Triphenylene-Bridged Trinuclear Complexes of Cu: Models for Spin Interactions in Two-Dimensional Electrically Conductive Metal-Organic Frameworks. *J. Am. Chem. Soc.* **2019**, *141*, 10475−10480.
(29) Sheberla, D.; Sun, L.; Blood-Forsythe, M. A.; Er, S.; Wade, C. R.; Brozek, C. K.; Aspuru-Guzik, A.; Dincă, M. High Electrical Conductivity in $Ni_3(2,3,6,7,10,11\text{-Hexaiminotriphenylene})_2$, a Semiconducting Metal-Organic Graphene Analogue. *J. Am. Chem. Soc.* **2014**, *136*, 8859−8862.
(30) Chen, S.; Dai, J.; Zeng, X. C. Metal-Organic Kagome Lattices $M_3(2,3,6,7,10,11\text{-Hexaiminotriphenylene})_2$ (M = Ni and Cu): From Semiconducting to Metallic by Metal Substitution. *Phys. Chem. Chem. Phys.* **2015**, *17*, 5954−5958.
(31) Sun, F.; Chen, X. Oxygen Reduction Reaction on $Ni_3(HITP)_2$: A Catalytic Site That Leads to High Activity. *Electrochem. Commun.* **2017**, *82*, 89−92.
(32) Miner, E. M.; Fukushima, T.; Sheberla, D.; Sun, L.; Surendranath, Y.; Dincă, M. Electrochemical Oxygen Reduction Catalysed by $Ni_3(Hexaiminotriphenylene)_2$. *Nat. Commun.* **2016**, *7*, 10942.
(33) He, Y.; Talin, A. A.; Allendorf, M. D. Thermoelectric Properties of 2D $Ni_3(hitp)_2$ and 3D $Cu_3(btc)_2$ MOFs: First-Principles Studies. *ECS J. Solid State Sci. Technol.* **2017**, *6*, N236.
(34) Tie, D. Y.; Chen, Z. First Principles Study of the Electronic Properties of a $Ni_3(2,3,6,7,10,11\text{-Hexaaminotriphenylene})_2$ Monolayer under Biaxial Strain. *RSC Adv.* **2015**, *5*, 55186−55190.
(35) Sheberla, D.; Bachman, J. C.; Elias, J. S.; Sun, C.-J.; Shao-Horn, Y.; Dincă, M. Conductive MOF Electrodes for Stable Supercapacitors with High Areal Capacitance. *Nat. Mater.* **2017**, *16*, 220−224.
(36) Le, K. N.; Hendon, C. H. Pressure-Induced Metallicity and Piezoreductive Transition of Metal-Centres in Conductive 2-Dimensional Metal-Organic Frameworks. *Phys. Chem. Chem. Phys.* **2019**, *21*, 25773−25778.
(37) Murase, R.; Leong, C. F.; D'Alessandro, D. M. Mixed Valency as a Strategy for Achieving Charge Delocalization in Semiconducting

https://doi.org/10.1021/acsaelm.0c01135
ACS Appl. Electron. Mater. 2021, 3, 2017−2023

and Conducting Framework Materials. *Inorg. Chem.* **2017**, *56*, 14373−14382.
(38) Foster, M. E.; Sohlberg, K.; Spataru, C. D.; Allendorf, M. D. Proposed Modification of the Graphene Analogue $Ni_3(HITP)_2$ To Yield a Semiconducting Material. *J. Phys. Chem. C* **2016**, *120*, 15001−15008.
(39) Karagiaridi, O.; Bury, W.; Tylianakis, E.; Sarjeant, A. A.; Hupp, J. T.; Farha, O. K. Opening Metal-Organic Frameworks Vol. 2: Inserting Longer Pillars into Pillared-Paddlewheel Structures through Solvent-Assisted Linker Exchange. *Chem. Mater.* **2013**, *25*, 3499−3503.
(40) Karagiaridi, O.; Bury, W.; Mondloch, J. E.; Hupp, J. T.; Farha, O. K. Solvent-Assisted Linker Exchange: An Alternative to the De Novo Synthesis of Unattainable Metal-Organic Frameworks. *Angew. Chem., Int. Ed.* **2014**, *53*, 4530−4540.
(41) Schneider, C.; Bodesheim, D.; Keupp, J.; Schmid, R.; Kieslich, G. Retrofitting Metal-Organic Frameworks. *Nat. Commun.* **2019**, *10*, 4921.
(42) Schneider, C.; Bodesheim, D.; Ehrenreich, M. G.; Crocellà, V.; Mink, J.; Fischer, R. A.; Butler, K. T.; Kieslich, G. Tuning the Negative Thermal Expansion Behavior of the Metal-Organic Framework Cu_3BTC_2 by Retrofitting. *J. Am. Chem. Soc.* **2019**, *141*, 10504−10509.
(43) Kapustin, E. A.; Lee, S.; Alshammari, A. S.; Yaghi, O. M. Molecular Retrofitting Adapts a Metal-Organic Framework to Extreme Pressure. *ACS Cent. Sci.* **2017**, *3*, 662−667.
(44) Siemensmeyer, K.; Peeples, C. A.; Tholen, P.; Schmitt, F.-J.; Çoşut, B.; Hanna, G.; Yücesan, G. Phosphonate Metal-Organic Frameworks: A Novel Family of Semiconductors. *Adv. Mater.* **2020**, *32*, 2000474.
(45) Kawamura, A.; Greenwood, A. R.; Filatov, A. S.; Gallagher, A. T.; Galli, G.; Anderson, J. S. Incorporation of Pyrazine and Bipyridine Linkers with High-Spin Fe(II) and Co(II) in a Metal-Organic Framework. *Inorg. Chem.* **2017**, *56*, 3349−3356.
(46) Ha, H.; Kim, Y.; Kim, D.; Lee, J.; Song, Y.; Kim, S.; Park, M. H.; Kim, Y.; Kim, H.; Yoon, M.; Kim, M. Effect of the Metal within Regioisomeric Paddle-Wheel-Type Metal-Organic Frameworks. *Chem. - Eur. J.* **2019**, *25*, 14414−14420.
(47) A. Manz, T. Introducing DDEC6 Atomic Population Analysis: Part 3. Comprehensive Method to Compute Bond Orders. *RSC Adv.* **2017**, *7*, 45552−45581.
(48) Ferey, G.; Mellot-Draznieks, C.; Serre, C.; Millange, F.; Dutour, J.; Surblé, S.; Margiolaki, I. A Chromium Terephthalate-Based Solid with Unusually Large Pore Volumes and Surface Area. *Science* **2005**, *309*, 2040−2042.
(49) Aziz, A.; Ruiz-Salvador, A. R.; Hernández, N. C.; Calero, S.; Hamad, S.; Grau-Crespo, R. Porphyrin-Based Metal-Organic Frameworks for Solar Fuel Synthesis Photocatalysis: Bandgap Tuning via Iron Substitutions. *J. Mater. Chem. A* **2017**, *5*, 11894−11904.
(50) Conradie, J. Jahn-Teller Effect in High Spin d^4 and d^9 Octahedral Metal-Complexes. *Inorg. Chim. Acta* **2019**, *486*, 193−199.
(51) Echigo, T.; Kimata, M. Single-Crystal X-Ray Diffraction and Spectroscopic Studies on Humboldtine and Lindbergite: Weak Jahn-Teller Effect of Fe^{2+} Ion. *Phys. Chem. Miner.* **2008**, *35*, 467.
(52) Zhang, X.; Lawson Daku, M. L.; Zhang, J.; Suarez-Alcantara, K.; Jennings, G.; Kurtz, C. A.; Canton, S. E. Dynamic Jahn-Teller Effect in the Metastable High-Spin State of Solvated $[Fe(Terpy)_2]^{2+}$. *J. Phys. Chem. C* **2015**, *119*, 3312−3321.
(53) Kresse, G.; Furthmüller, J. Efficient Iterative Schemes for Ab Initio Total-Energy Calculations Using a Plane-Wave Basis Set. *Phys. Rev. B: Condens. Matter Mater. Phys.* **1996**, *54*, 11169−11186.
(54) Perdew, J. P.; Ruzsinszky, A.; Csonka, G. I.; Vydrov, O. A.; Scuseria, G. E.; Constantin, L. A.; Zhou, X.; Burke, K. Restoring the Density-Gradient Expansion for Exchange in Solids and Surfaces. *Phys. Rev. Lett.* **2008**, *100*, 136406.
(55) Jain, A.; Hautier, G.; Ong, S. P.; Moore, C. J.; Fischer, C. C.; Persson, K. A.; Ceder, G. Formation Enthalpies by Mixing GGA and GGA+U Calculations. *Phys. Rev. B: Condens. Matter Mater. Phys.* **2011**, *84*, 045115.
(56) Cococcioni, M.; de Gironcoli, S. Linear Response Approach to the Calculation of the Effective Interaction Parameters in the LDA+U Method. *Phys. Rev. B: Condens. Matter Mater. Phys.* **2005**, *71*, 035105.

https://doi.org/10.1021/acsaelm.0c01135
ACS Appl. Electron. Mater. 2021, 3, 2017−2023